CHAOS **27**, 093932 (2017)

Sensitivity of reentrant driver localization to electrophysiological parameter variability in image-based computational models of persistent atrial fibrillation sustained by a fibrotic substrate

Dongdong Deng,[a] Michael J. Murphy,[a] Joe B. Hakim, William H. Franceschi, Sohail Zahid,
Farhad Pashakhanloo, Natalia A. Trayanova, and Patrick M. Boyle[b]
Institute for Computational Medicine and Department of Biomedical Engineering, Johns Hopkins University, Baltimore, Maryland 21218, USA

(Received 3 April 2017; accepted 4 September 2017; published online 19 September 2017)

Atrial fibrillation (AF) is the most common sustained cardiac arrhythmia, causing morbidity and mortality in millions worldwide. The atria of patients with persistent AF (PsAF) are characterized by the presence of extensive and distributed atrial fibrosis, which facilitates the formation of persistent reentrant drivers (RDs, i.e., spiral waves), which promote fibrillatory activity. Targeted catheter ablation of RD-harboring tissues has shown promise as a clinical treatment for PsAF, but the outcomes remain sub-par. Personalized computational modeling has been proposed as a means of non-invasively predicting optimal ablation targets in individual PsAF patients, but it remains unclear how RD localization dynamics are influenced by inter-patient variability in the spatial distribution of atrial fibrosis, action potential duration (APD), and conduction velocity (CV). Here, we conduct simulations in computational models of fibrotic atria derived from the clinical imaging of PsAF patients to characterize the sensitivity of RD locations to these three factors. We show that RDs consistently anchor to boundaries between fibrotic and non-fibrotic tissues, as delineated by late gadolinium-enhanced magnetic resonance imaging, but those changes in APD/CV can enhance or attenuate the likelihood that an RD will anchor to a specific site. These findings show that the level of uncertainty present in patient-specific atrial models reconstructed without any invasive measurements (i.e., incorporating each individual's unique distribution of fibrotic tissue from medical imaging alongside an average representation of AF-remodeled electrophysiology) is sufficiently high that a personalized ablation strategy based on targeting simulation-predicted RD trajectories alone may not produce the desired result. *Published by AIP Publishing.*
[http://dx.doi.org/10.1063/1.5003340]

Millions of people are affected by potentially lethal cardiac arrhythmias, which are conditions that impair the heart's ability to regulate its own rhythm. Catheter ablation, in which radiofrequency energy is used to destroy specific areas of heart tissues responsible for arrhythmia perpetuation, provides permanent relief from symptoms in many patients. Success rates for these procedures remain sub-optimal in individuals with persistent atrial fibrillation (PsAF), because there is no consensus for deciding exactly which tissue should be ablated. Computational simulations conducted in atrial models derived from medical imaging scans of patient hearts have been proposed as a promising potential avenue for non-invasively identifying the optimal ablation targets in each individual, but many open questions regarding the predictive value of this approach remain unanswered. For example, it remains unclear how the locations of arrhythmia drivers targeted for catheter ablation are influenced by inter-patient differences in the spatial pattern of a disease-remodeled tissue (which can be ascertained by imaging) and variability in key electrophysiological tissue properties (which can only be obtained by invasive measurements). The results presented in this study demonstrate that arrhythmia drivers in personalized atrial models consistently localize to boundaries between fibrotic and non-fibrotic tissues regardless of variability in electrophysiological parameters, but that the specific anchoring sites that manifest are affected by the latter variability. Overall, our analysis indicates that the level of uncertainty present in patient-specific models generated solely from non-invasive imaging does not make the targeting of simulated trajectories of arrhythmia drivers only a reliable methodology for planning catheter ablation of persistent atrial fibrillation.

I. INTRODUCTION

Proper cardiac function relies on the organized conduction of electrical impulses in heart tissues. During a normal sinus rhythm, waves of electrical excitation emanate from the sinoatrial node and traverse the atria before propagating through the atrioventricular node and Purkinje fibers to activate ventricular tissues.[1] During this excitation sequence, atrial contraction ensures optimal filling of the ventricles. Thus, orderly contraction of the atria is necessary for efficient cardiac function. However, in some pathological cases,

---

[a] D. Deng and M. J. Murphy contributed equally to this paper.
[b] Author to whom correspondence should be addressed: pmjboyle@jhu.edu, Tel.: (410) 516-3322, Fax: (410) 516-5294.

this sequence of electrical activation is disrupted, resulting in irregular heartbeats, inefficient mechanical contraction, and increased risk of stroke.[1]

Atrial fibrillation (AF), which is characterized by asynchronous and chaotic beating of the atria, is the most prevalent sustained cardiac arrhythmia, causing morbidity and mortality in over 3×10^6 people in the United States alone.[2] This disease is further complicated by its progressive nature: each year, 5% of AF patients develop persistent AF (PsAF) due to electrophysiological and fibrogenic remodeling of atrial tissues.[3] PsAF is characterized by arrhythmia episodes that last $\geq$7 days, and treatment options are extremely limited.[1] Recent evidence suggests that PsAF is sustained partly by persistent spiral waves [i.e., reentrant drivers (RDs)] that promote fibrillatory activity.[4–6] The underlying organizing centers of RDs, which can be identified by tracking wavefront tip trajectories or identifying phase singularities, meander within tissue regions that are spatially compact ($\sim$1–2 cm^2, $\sim$7 mm in length).[5–8]

The fibrotic substrate in PsAF patients involves both changes in the extracellular matrix and electrophysiological remodeling in myocytes within the fibrotic tissue.[3,9] Improved understanding of how fibrotic substrate characteristics influence RD localization dynamics would facilitate the development of better treatments for PsAF, since organizing centers have been proposed as targets for custom-tailored catheter ablation.[5,6] Unfortunately, such insights have proved difficult to attain due to significant inter-patient variability in the two distinct components of the fibrotic substrate: (1) spatial distribution of the fibrotic tissue in the atria (i.e., structural component)[10,11] and (2) electrophysiological properties of the affected atrial tissue, such as action potential duration (APD) and conduction velocity (CV) (i.e., functional component).[12–16] No study to date has attempted to determine how these sources of variability influence RD localization.

Thus, our objective was to systematically assess the relative influence of structural and electrophysiological components of the atrial fibrotic substrate, as described above, on RD localization dynamics in PsAF. Towards this goal, we conducted simulations in computational models derived from late gadolinium-enhanced magnetic resonance imaging (LGE-MRI) scans of the fibrotic atria of PsAF patients. AF was induced in models with either average human AF electrophysiology or with variations in electrophysiological properties, and differences in RD localization dynamics were analyzed. Establishing how these dynamics are affected by electrophysiological variability is important from a clinical standpoint, since it will provide information about the level of uncertainty inherent in atrial fibrosis models reconstructed from non-invasive patient imaging data only. Specifically, it will determine whether an ablation planning based solely on targeting the trajectories of RDs predicted by simulations conducted in such models would be a viable approach.

II. METHODS

A. Patient specific atrial models

In this study, we used 12 biophysically realistic patient-specific models derived from LGE-MRI scans acquired for individuals with PsAF, which is uninterrupted AF lasting longer than seven days.[17] Details regarding patient information and model construction can be found in our previous publications.[7,18,19] Briefly, regions of fibrotic and non-fibrotic myocardium were segmented out from clinical scans using a validated algorithm based on the image intensity ratio,[20] and fiber orientations were assigned using an image-based estimation approach.[7,18,21–24] We used the latter approach since, although *ex vivo* MRI of human atria has been performed,[25] no method currently exists that is capable of non-invasively measuring coupling anisotropy in the human heart.

B. Modeling cell- and tissue-scale variability of atrial electrophysiology

The approach to represent the propagation of biophysical excitation in the fibrotic atria of PsAF patients has been described comprehensively in our earlier work.[7,18] Model parameters controlling myocyte membrane kinetics and anisotropic conduction velocities within fibrotic and non-fibrotic regions were calibrated to match relevant experimental recordings. In non-fibrotic regions, membrane kinetics were represented with a human atrial model under chronic AF conditions;[26,27] in fibrotic regions, additional changes were made to represent changes due to fibrogenic remodeling: −50% I_{K1}, −50% I_{CaL}, −40% I_{Na}.[28–30] Conductivity values were calibrated to obtain a longitudinal CV of 43.39 cm/s in non-fibrotic tissues, consistent with the CV observed via high-density mapping of electrically-induced AF during open-heart surgery in human patients;[31] the conductivity in fibrotic regions was reduced by 30% to represent changes in the extracellular matrix composition, resulting in a longitudinal CV of 20 cm/s.[32,33] Finally, since fibrosis slows CV more dramatically in the direction transverse to cardiac fibers, the longitudinal-to-transverse anisotropy ratio was increased from 5:1 in non-fibrotic to 8:1 in fibrotic regions.[32,33]

To establish baseline RD localization dynamics in the absence of variability in the electrophysiological component of the fibrotic substrate, we first conducted simulations under average human AF electrophysiology, as in previous studies.[7,18] For brevity, these conditions are referred to as EP_{avg}. We then ran simulations in atrial models with the same geometric structure and fibrotic tissue distribution to assess the effects of APD and CV variability. We focused exclusively on these two properties because they are known to affect multiple emergent phenomena relevant to arrhythmia dynamics, including refractoriness periods, wavebreak incidence, and RD stability.[34–36] For simulations with APD variability, specific ionic currents were modified to achieve ±10% APD [Figs. 1(a) and (b)], while minimally altering other AP properties, including resting membrane potential [V_m], AP amplitude, and restitution curve slope [Figs. 1(c) and 1(d)]. Since we were concerned about variability in intrinsic APD, these experiments were conducted in isolated cell-scale models. For simulations with CV variability, the longitudinal and transverse components of the conductivity tensor were modified to achieve ±10% CV. To avoid biasing effects from the complex fibrous structure in atrial models,

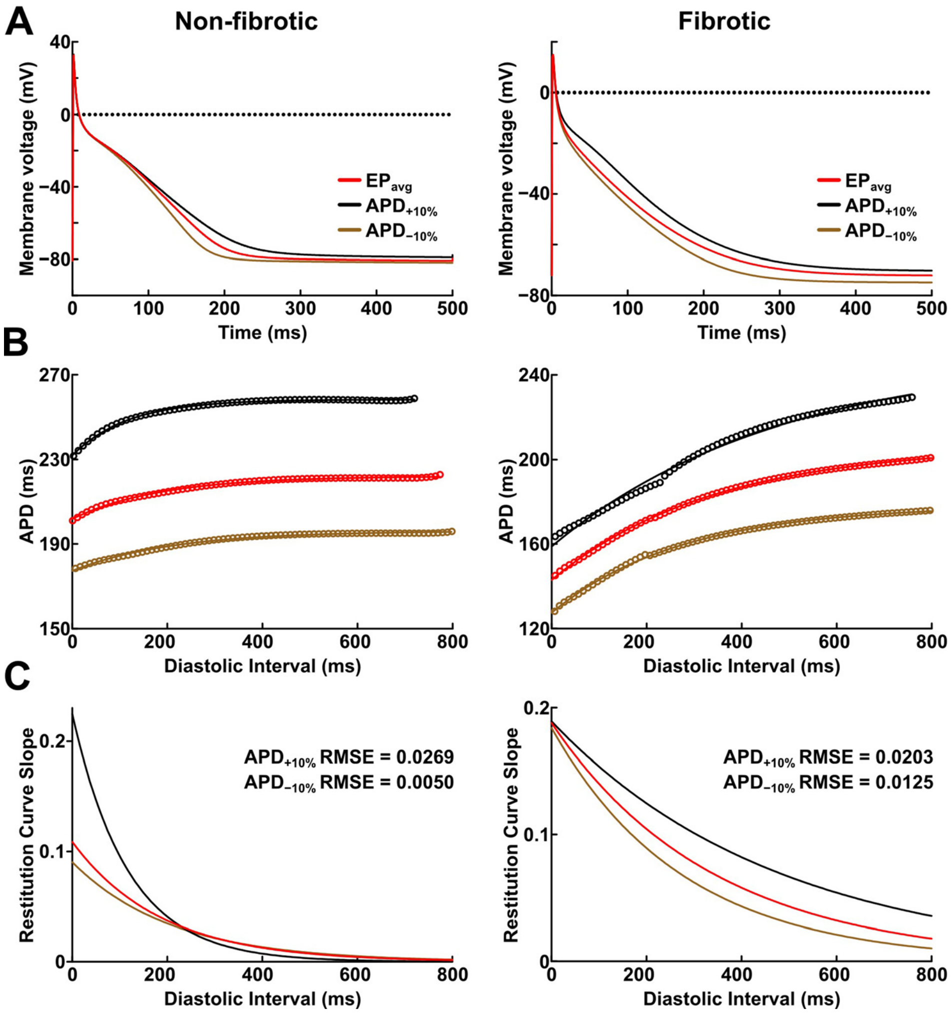

FIG. 1. (a) Action potential (AP) traces for simulated non-fibrotic (left) and fibrotic (right) atrial myocytes, paced to steady-state (1000 stimuli at basic cycle length = 500 ms) under average human AF electrophysiology (EP_{avg}) conditions and with AP duration (APD) variability (±10%). (b) APD restitution relationships for the respective cell types shown in A. Fit lines obtained via exponential regression. (c) Plots showing APD restitution curve slope values for different diastolic intervals. Root mean squared error (RMSE) values between $APD_{\pm 10\%}$ and EP_{avg} curves are shown.

CV values were calibrated by simulating the stimulation of the center point of a slab model (6 cm × 6 cm × 2.7 mm) with uniform fiber orientations, and conductivity tensor values were adjusted until the desired longitudinal and transverse CVs were observed. In both cases (i.e., $APD_{\pm 10\%}$ and $CV_{\pm 10\%}$ conditions), parameter changes required to achieve the desired emergent property were different for non-fibrotic and fibrotic tissues. Complete details about these changes and the resulting variability in APD and CV are presented in Tables I and II, respectively.

TABLE I. Cell-scale electrophysiological model parameters modified to achieve ±10% action potential duration (APD) in non-fibrotic and fibrotic atrial tissues. "…" indicates no change. EP_{avg}: average human AF electrophysiology; APA: action potential amplitude; V_{rest}: resting membrane potential; I_{K1}: inward rectifier potassium current; I_{Kr}: rapid delayed rectifier potassium current; and I_{CaL}: L-type calcium current.

		Parameters changed		APD (ms)	APA (mV)	V_{rest} (mV)
Non-fibrotic	$APD_{-10\%}$	$+20\%\ I_{K1}$	$+10\%\ I_{Kr}$	163.5	114.16	−82.03
	EP_{avg}	…	…	181.8	113.45	−80.84
	$APD_{+10\%}$	$-20\%\ I_{K1}$	…	200.0	112.09	−78.96
Fibrotic	$APD_{-10\%}$	$-30\%\ I_{CaL}$	$+20\%\ I_{K1}$	194.8	95.54	−75.56
	EP_{avg}	…	…	216.3	88.76	−72.05
	$APD_{+10\%}$	$+60\%\ I_{CaL}$	$-10\%\ I_{K1}$	238.1	77.82	−68.15

Notably, the model systems used to calibrate parameter changes for models with APD/CV variability had reduced the scale and geometric complexity compared to the atrial models used in subsequent simulations. As such, it should be stressed that incorporation of these parameters in the latter models does not guarantee the same degree of electrophysiological changes, since organ-scale APD/CV are emergent properties that depend on both the intrinsic properties we directly manipulated and other factors, including atrial shape, fiber orientations, and electrotonic coupling between tissues within and between fibrotic and non-fibrotic regions.

C. Assessing the effects of APD and CV variability on RD localization

First, the inducibility of PsAF-perpetuating RDs sustained by the fibrotic substrate in each patient-specific atrial model under EP_{avg} conditions was assessed by applying rapid electrical pacing (with a clinically relevant programmed stimulation sequence[37]) from 30 locations evenly distributed in the left and right atria, as in our original study.[7] The outcome of pacing was classified as arrhythmia if the last pacing stimulus was followed by at least 2000 ms of self-sustaining RD activity. Since our models do not include sinoatrial node excitation or triggered activity, any activity that persists during the latter interval must be reentry-driven

TABLE II. Tissue-scale electrophysiological model parameters modified to achieve ±10% longitudinal and transverse conduction velocities (CV_L and CV_T, respectively) in non-fibrotic and fibrotic atrial tissues. "…" indicates no change. σ_{iL} and σ_{iT}: longitudinal and transverse conductivity tensor values. EP_{avg}: average human AF electrophysiology.

		Parameters changed		CV_L (cm/s)	CV_T (cm/s)	CV_L: CV_T
Non-fibrotic	$CV_{-10\%}$	$-17\%\ \sigma_{iL}$	$-16\%\ \sigma_{iT}$	41.5	12.6	3.29
	EP_{avg}	…	…	46.3	14.8	3.13
	$CV_{+10\%}$	$+18\%\ \sigma_{iL}$	$+20\%\ \sigma_{iT}$	50.9	17.1	2.98
Fibrotic	$CV_{-10\%}$	$-16\%\ \sigma_{iL}$	$-15\%\ \sigma_{iT}$	19.4	3.3	5.88
	EP_{avg}	…	…	21.7	4.1	5.29
	$CV_{+10\%}$	$+15\%\ \sigma_{iL}$	$+16\%\ \sigma_{iT}$	23.8	4.8	4.96

by definition. Cases in which macro-reentry around non-conductive orifices (e.g., pulmonary vein borders, mitral/tricuspid valves, etc.) were classified as atrial tachycardia and not included in our analysis of RD-perpetuated AF. Subsequently, to probe the effect of APD/CV variability on RD localization, the subset of pacing sequences that induced RDs under EP_{avg} conditions was repeated in the same atrial models under $APD_{\pm 10\%}$ and $CV_{\pm 10\%}$ conditions. Finally, in all atrial models, under all electrophysiological conditions (EP_{avg}, $APD/CV_{\pm 10\%}$), we repeated the above protocol for a new set of 15 biatrial pacing sites, distinct from the original pacing locations, to account for the possibility that some pacing sites might induce AF in $APD/CV_{\pm 10\%}$ simulations, but not under EP_{avg} conditions.

In all cases of induced AF, the tissue region within which the organizing centers of the AF-perpetuating RD meandered was identified using an approach based on the analysis of dynamic wavefront tip trajectory. First, the extrema of the tip trajectory (i.e., the "pivot points" of the RD wavefront) were identified during a 1000 ms analysis interval at the end of each AF simulation; this temporal window ensured that multiple RD rotations were analyzed and that any transient instability observed shortly after AF initiation was ignored. Then, RD location was defined as the midpoint between the extrema. We used this empirical approach because we found it as faster and less sensitive to false positives (i.e., transient non-RD activity incorrectly classified as RD) compared to the phase singularity-based method we have used previously.[7] The ablation target corresponding to each observed RD trajectory was defined by identifying the surrounding tissue volume within 3.5 mm (i.e., the ablation lesion radius for standard irrigated-tip catheters).[6]

Two approaches were used to quantitatively compare RD targets from $APD_{\pm 10\%}$ and $CV_{\pm 10\%}$ simulations with those observed under EP_{avg} conditions. First, we calculated the degree of volumetric overlap between RD targets induced under variable APD/CV conditions and all of the RD targets observed during EP_{avg} simulations in the same atrial model. Second, we identified the centroid of each RD target volume defined d_{RD} as the distance between the centroids of the $APD/CV_{\pm 10\%}$ RD target, the nearest target observed during EP_{avg} simulations. To put our findings in a clinical perspective, d_{RD} values were compared to the typical ablation lesion diameter (~7 mm).[6]

All electrophysiological simulations were conducted using the CARP software package (Cardiosolv, LLC)[38,39] on a high performance parallel computing system. Each second of simulated activity required ~30 min of computing time in 24 Intel Xeon CPU cores (2.80 GHz) in parallel. The total computational burden for all simulations discussed in this paper was >60 000 h of CPU time.

III. RESULTS

For simulations conducted under EP_{avg} conditions, rapid pacing induced AF sustained by stable RDs in all 12 patient-specific atrial models; data for these cases are summarized in Table III. There were between 1 and 14 total RDs (6.3 ± 4.1) induced in each model, and these RDs were located in between 2 and 8 (4.1 ± 2.3) spatially distinct locations (i.e., with non-overlapping RD trajectories). The extent of simulated ablation required to surround all RD trajectories (3.5 mm lesion radius) was 1.85 ± 0.95% of the total atrial volume (min: 0.36%, max: 3.31%). For all cases observed in EP_{avg} simulations, the RD cycle length was 278.6 ± 50.6 ms.

Comprehensive summary data for RDs observed in simulations conducted in all 12 atrial models under $APD/CV_{\pm 10\%}$ conditions are provided in the supplementary material, Tables S1–S4. RD cycle lengths observed in these simulations were as follows: 283.5 ± 53.2 ms ($APD_{+10\%}$; mean + 1.8% compared to EP_{avg}), 262.9 ± 44.4 ms ($APD_{-10\%}$; −5.6%), 265.3 ± 46.6 ms ($CV_{+10\%}$; −4.8%), and 278.8 ± 58.4 ms ($CV_{-10\%}$; +0.1%). RDs were induced for all four EP parameter variants in 9/12 patient models. For P9, RD initiation was only observed under the $APD_{+10\%}$ condition, while for P11 and P12, there was a single condition ($APD_{+10\%}$ and $APD_{-10\%}$, respectively) in which AF could not be initiated. Notably, for the latter three models, the number of distinct RDs initiated under EP_{avg} conditions was also low (see Table III). Under the $APD_{+10\%}$ condition, 35% (18/52) of observed RD trajectories had an ablation target that partially coincided with an EP_{avg} target. For this subset of cases, the rate of overlap was 57.3 ± 26.0% [Fig. 2(a)] and d_{RD} was 5.2 ± 4.4 mm [Fig. 2(b)]. For the remaining (non-overlapping) RD trajectories, d_{RD} was 42.9 ± 14.3 mm [Fig. 2(c)]. For the other three

TABLE III. Summary of results for simulations conducted in EP_{avg} models. RDs were classified as being part of the same distinct RD site if their trajectories overlapped.

ID	# RDs	# distinct RD sites	Extent of ablated tissue (%)
P01	14	8	3.3
P02	9	5	2.7
P03	7	5	1.7
P04	9	8	2.8
P05	6	4	2.3
P06	3	2	1.0
P07	2	2	1.3
P08	9	5	2.6
P09	1	1	0.4
P10	10	4	2.4
P11	3	3	1.0
P12	2	2	0.7

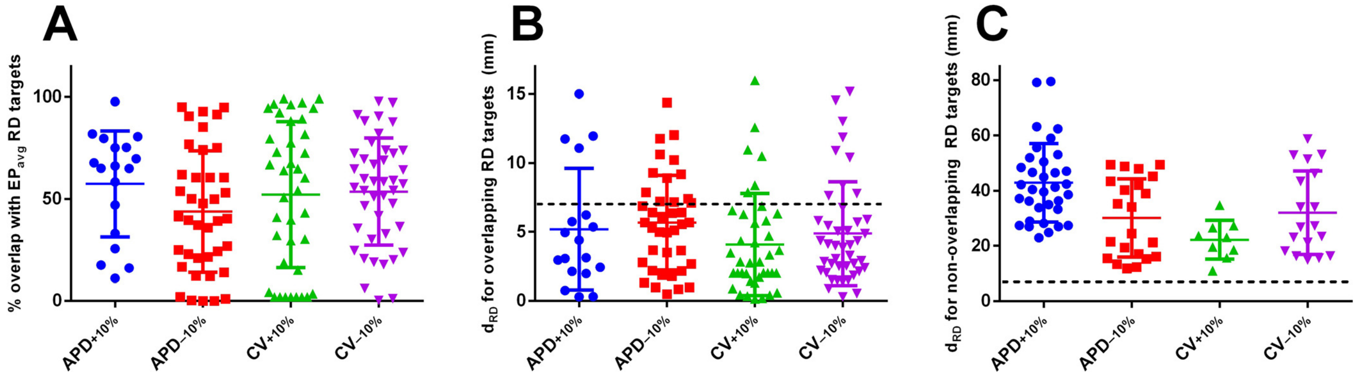

FIG. 2. Summary of quantitative reentrant driver (RD) analysis. (a) Each point represents the degree of overlap between an ablation target associated with an RD observed in simulations with EP parameter variation and the nearest target from EP_{avg} cases. Points with exactly zero overlap are omitted for ease of visualization. n = 18, 39, 33, and 44 from left to right. (b) For the same subset of RDs considered in (a), d_{RD} distance metric values (see text) are plotted. Dashed line indicates $d_{RD} = 7$ (i.e., distance corresponding to a typical ablation lesion diameter). (c) Same as (b), but for RD targets observed in APD/$CV_{\pm 10\%}$ simulations where there was no overlap with any EP_{avg} target. n = 34, 22, 9, and 18 from left to right. Horizontal lines show mean ±SD.

EP variants (data also shown in Fig. 2), the values were as follows: $APD_{-10\%}$: 64% (39/61) with 43.8 ± 29.9% overlap and $d_{RD} = 5.7 \pm 3.4$ mm, non-overlapping $d_{RD} = 30.1 \pm 14.2$ mm; $CV_{+10\%}$: 79% (33/42) with 63.0 ± 29.7% overlap and $d_{RD} = 4.5 \pm 3.9$ mm, non-overlapping $d_{RD} = 22.2 \pm 7.0$ mm; and, $CV_{-10\%}$: 70% (43/61) with 53.6 ± 26.3% overlap and $d_{RD} = 4.9 \pm 3.8$ mm, $d_{RD} = 32.0 \pm 15.1$ mm. Overall, for the subset of overlapping RD targets observed in APD/$CV_{\pm 10\%}$ simulations, 48.2% had $d_{RD} \leq 7$ mm [dashed line in Fig. 2(b)], indicating that the RD trajectories were within the diameter of a single ablation lesion (breakdown by variability type: $APD_{+10\%}$: 26.9%, $APD_{-10\%}$: 42.6%, $CV_{+10\%}$: 68.8%, $CV_{-10\%}$: 55.7%). In contrast, among non-overlapping RDs, no d_{RD} values less than 7 mm were observed at all [Fig. 2(c)].

Schematics showing the distribution of fibrotic tissues and the degree of overlap between RD targets from simulations with APD/$CV_{\pm 10\%}$ and EP_{avg} are shown for all 12 models in Fig. 3 and Figs. S1–S11. Consistent with the quantitative results summarized in the preceding paragraph, in each patient model, under each variable EP condition, some RDs had associated targets that overlapped considerably with EP_{avg} RD targets, while others were observed in completely different locations. Interestingly, regardless of the EP conditions used to conduct simulations, we observed that RD trajectories were always within or near boundary regions between fibrotic and non-fibrotic tissues (i.e., solid black outlines in Fig. 3 and Figs. S1–S11). This behavior was observed in our previous study,[7] which was conducted exclusively in EP_{avg} models.

For the specific example shown in Fig. 3, all four panels show 14 EP_{avg} targets in 8 regions: two in the posterior left atrium (LA), two near the right pulmonary veins (PVs), one in the superior atrium (RA) on the superior vena cava (SVC); and three in inferior RA near the inferior vena cava (IVC). The $APD_{+10\%}$ panel (A) shows two overlapping RD targets (gold highlighted regions) in the right PVs and two emergent RD targets that were never seen in EP_{avg} simulations, one on the other side of the right PVs and the other in the lateral RA. The $APD_{-10\%}$ panel (B) shows overlapping RD targets in the posterior RA, right PVs, inferior RA (multiple targets) along with emergent RDs in the left PVs and the SVC. The $CV_{+10\%}$ panel (C) shows three RD targets that were of extremely close match to EP_{avg} cases (posterior LA, IVC, and inferior RA; ∼100% overlap in all cases); however, emergent RD targets were also seen in the infero-posterior LA, the lateral RA, and the right PVs. Intriguingly, the latter case (marked by *) was nearly identical to an emergent RD target observed in the $APD_{+10\%}$ and $CV_{-10\%}$ cases, indicating that some atrial regions with a robust propensity for RD localization did not give rise to RDs in EP_{avg}

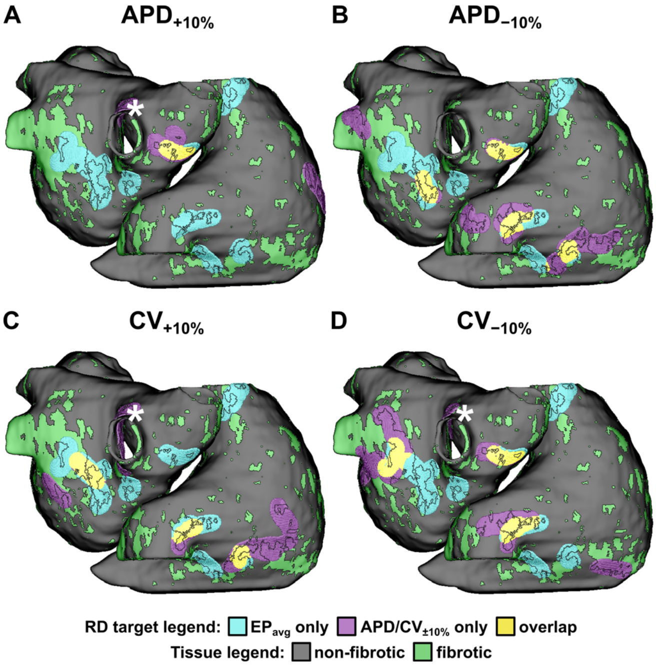

FIG. 3. Schematic showing the distribution of fibrotic tissues and the degree of overlap between RD targets from simulations with EP parameter variation and EP_{avg} cases for one atrial model (P01). Similar schematics for all 11 other atrial models can be found in the supplementary material (Figs. S1–S11). RD targets are defined as the volume within 3.5 mm surrounding each observed RD trajectory. Fibrotic tissue regions (green) are shown, with boundaries (black lines) superimposed on RD targets to facilitate the visualization of RD trajectories with respect to patient-specific spatial pattern of remodeling. * indicates the ablation target for an RD in the right pulmonary vein area that emerged under 3/4 variable EP conditions, but never in simulations with EP_{avg}.

simulations under the current protocol. Finally, the $CV_{-10\%}$ panel (D) shows multiple overlapping RD targets in three regions (posterior LA, left PVs, IVC) along with emergent RDs in the left and right PVs, the latter of which was in the same area noted in the preceding analysis of $CV_{+10\%}$ cases (*).

Figure 4 presents activation maps corresponding to specific examples in which applying the same electrical stimuli under EP_{avg} and variable APD/CV conditions resulted in the initiation of AF sustained by RDs in very similar locations (within the radius of a single ablation lesion, i.e., $d_{RD} < 3.5\,mm$[6]). In the first case [Fig. 4(a)], the distance between RD locations observed in the EP_{avg} and $APD_{+10\%}$ simulations was $d_{RD} = 3.21\,mm$. Both RDs were located on the anterior side of the LA with a clockwise wavefront propagation pattern and a tip trajectory that ran parallel to the base of the LA appendage. In the second case [Fig. 4(b)], the RD locations observed in the EP_{avg} and $APD_{-10\%}$ simulations were essentially identical (i.e., $d_{RD} \approx 0$), with counterclockwise wavefront propagation on the postero-lateral LA and a tip trajectory that ran parallel to the ridge running beneath the left superior and inferior pulmonary veins. In the third case [Fig. 4(c)], the distance between RD locations observed in the EP_{avg} and $CV_{+10\%}$ simulations was $d_{RD} = 0.89\,mm$. In both cases, the RD was located in the postero-inferior LA with a counterclockwise rotation and a tip trajectory that ran parallel to the annulus of the mitral valve. In the fourth example [Fig. 4(d)], the distance between RDs observed in the EP_{avg} and $CV_{-10\%}$ simulations was $d_{RD} = 2.27\,mm$. Both RDs were located in the posterior LA between the left and right inferior pulmonary veins, with clockwise wavefront propagation and a relatively compact tip trajectory.

Interestingly, although all four of the cases shown in Fig. 4 highlighted examples where RD localization dynamics were insensitive to variability in APD and CV, we observed differences in macroscopic arrhythmia characteristics in models under different electrophysiological conditions. These differences were assessed in qualitative terms by examining cases in which RD trajectories in EP_{avg} and $APD/CV_{\pm 10\%}$ were at least partially overlapping, but the activation sequence in the periphery (i.e., distal to the RD trajectory) was distinct. For example, the $APD_{-10\%}$ panel of Fig. 4(b) shows a clear example of a transient conduction block near the left inferior pulmonary vein that is conspicuously absent from the corresponding EP_{avg} panel. In the other three cases shown in Fig. 4, the size and the extent of regions of block were variable between EP_{avg} and variable APD/CV simulations. This observation was reflective of a common trend in the subset of cases where APD/CV variability had only minor effects on RD localization (35%–79% depending on the EP variant): despite the fact that RD trajectories overlapped considerably, there were consistent differences in the peripheral activation sequence outside the AF driver region.

Figure 5 highlights two cases in which the same stimulus induced AF under all five electrophysiological conditions tested (EP_{avg}, $APD_{\pm 10\%}$, and $CV_{\pm 10\%}$). In the first example [Fig. 5(a)], all five panels show AF episodes driven by an RD located in the posterior LA, near the left inferior pulmonary

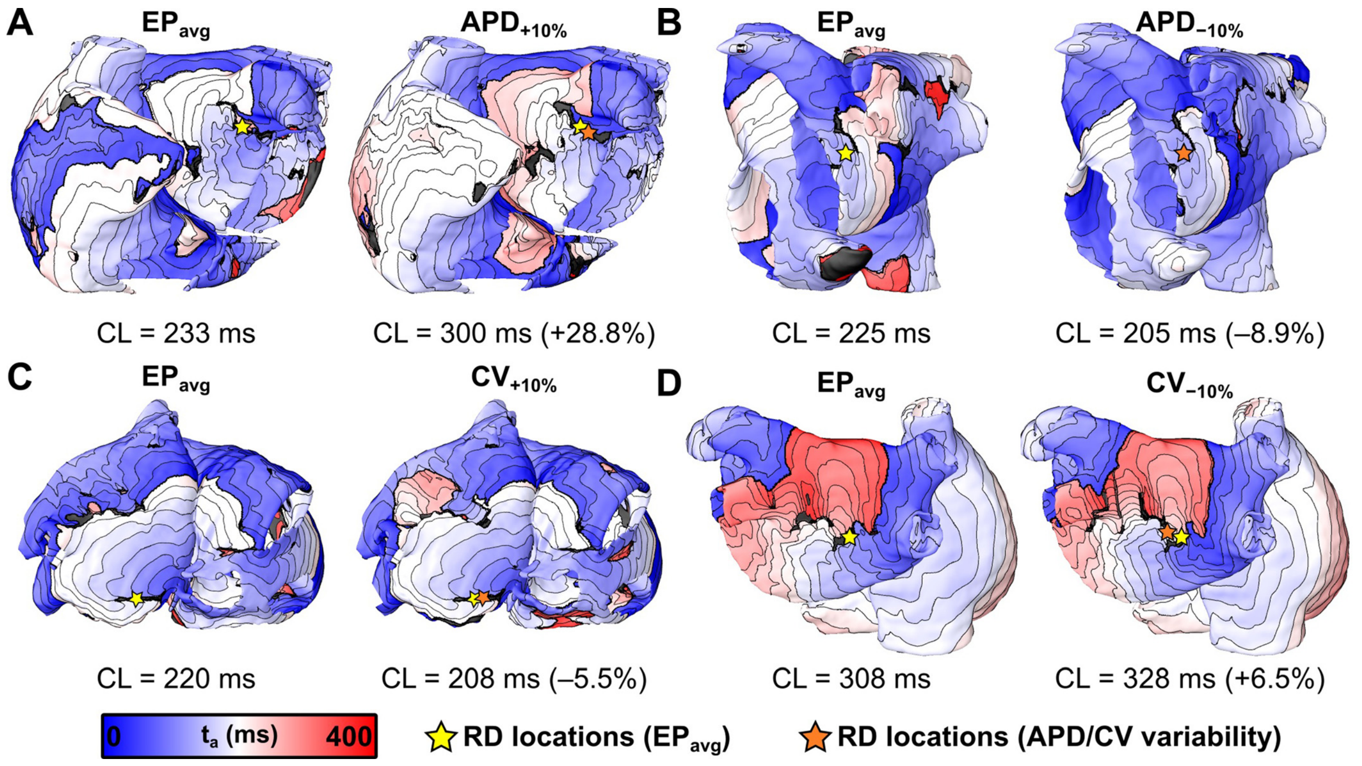

FIG. 4. 3-dimensional maps of activation time (t_a) showing locations of RDs induced by the same rapid pacing stimuli applied in the same patient-specific models under average human AF electrophysiology (EP_{avg}) (left) and variable APD/CV (right) conditions. Spacing between isochrones is 20 ms in all cases. Cycle length (CL) values are provided under each map and the relative change (%) between $APD/CV_{\pm 10\%}$ and EP_{avg} models are shown. (a) and (b) RDs located in region 1 (left pulmonary veins and atrial appendage) of P03 and P06 models, respectively. (c) RDs located in region 3 (inferior left atrium) of P10 model. (d) RDs located in region 2 (right pulmonary veins) of P08 model.

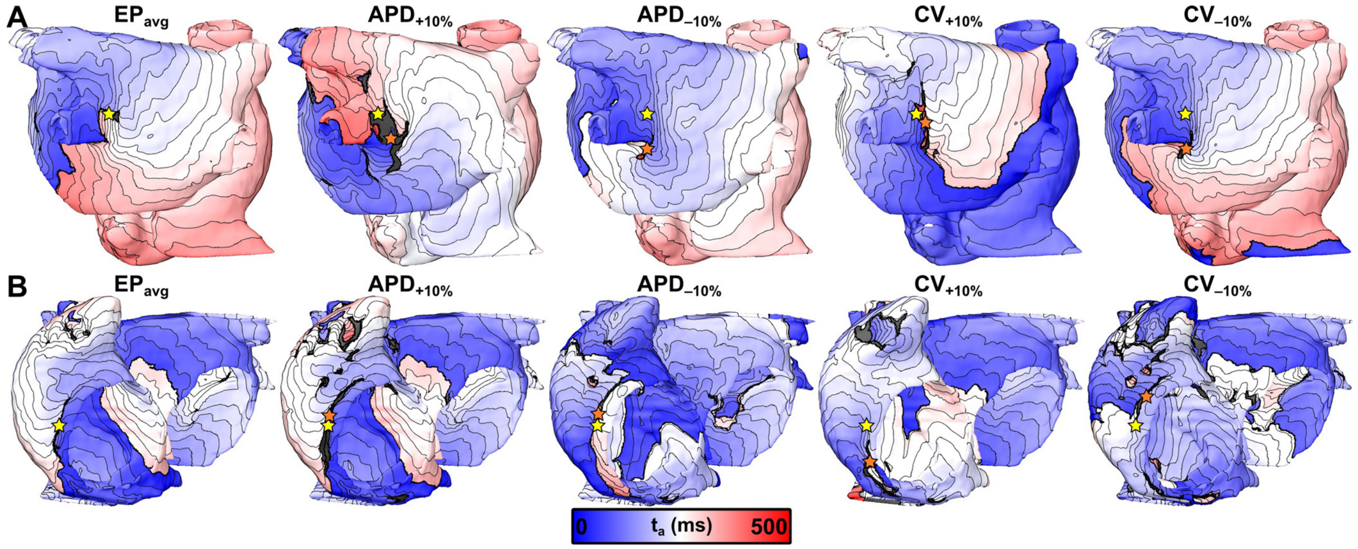

FIG. 5. Activation maps, following the same convention as Fig. 4, highlighting two cases in which the same pacing sequence applied in the same model led to the initiation of AF driven by an RD in the same atrial region, regardless of the variability in APD/CV. (a) RDs located in region 1 (left pulmonary veins) of P02 model. (b) RDs located in region 5 (inferior right atrium) of P04 model.

vein. Distances between RDs induced under variable APD/CV and EP$_{avg}$ conditions were relatively small: APD$_{+10\%}$: $d_{RD} = 15.2$ mm; APD$_{-10\%}$: $d_{RD} = 16.4$ mm; CV$_{+10\%}$: $d_{RD} = 5.78$ mm; and CV$_{-10\%}$: $d_{RD} = 17.39$ mm. The second example, shown in Fig. 5(b), features five RDs induced under different conditions, all located in the infero-lateral RA. All of these RDs had a relatively long tip trajectory (>1 cm) that ran parallel to the annulus of the tricuspid valve. As in the previous case [i.e., Fig. 5(a)], the RD distances for variable APD/CV cases were relatively small: APD$_{+10\%}$: $d_{RD} = 4.02$ mm; APD$_{-10\%}$: $d_{RD} = 4.09$ mm; CV$_{+10\%}$: $d_{RD} = 11.8$ mm; and CV$_{-10\%}$: $d_{RD} = 9.45$ mm.

Similar to cases discussed above, differences between activation sequences distal to RD locations in Figs. 5(a) and 5(b) show aspects of organ-scale excitation distal to the RD, and in these cases, they were affected by EP parameter modulation [e.g., transient reentry inferior to left inferior pulmonary vein in the APD$_{+10\%}$ panel of Fig. 5(a); regions of block near RA appendage in the APD$_{+10\%}$ panel of Fig. 5(b); heterogeneous excitation patterns, including conduction block and transient reentry, in APD$_{-10\%}$ and CV$_{-10\%}$ panels of Fig. 5(b)]. Moreover, in these cases, we observed examples where RD locations were the same as in simulations with EP$_{avg}$, but RD chirality was reversed [e.g., APD$_{+10\%}$ in Fig. 5(a); APD$_{-10\%}$, CV$_{+10\%}$, and CV$_{-10\%}$ in Fig. 5(b)].

One final example shows an interesting case (Fig. 6), in which the same rapid pacing stimulus applied in simulations conducted under EP$_{avg}$ and CV$_{-10\%}$ conditions initiated RDs in completely different atrial regions (EP$_{avg}$: antero-inferior wall of RA; CV$_{-10\%}$: lateral LA, near ridge below left pulmonary veins). Interestingly, in the EP$_{avg}$ case, we observed transient instances of conduction block and wavefront collision (highlighted by yellow arrows in the left panel of Fig. 6) in the location where the AF-sustaining RD was induced under CV$_{-10\%}$ conditions. This suggests that under different circumstances (e.g., following modification of the existing substrate via catheter ablation), that site might have emerged as a new potential RD location in EP$_{avg}$ simulations, even though it was not identified during the initial round of simulations. Notably, even though the RD locations shown in this example were quite far apart (∼80 mm), the corresponding d_{RD} value was 33.96 mm because the RD induced under the CV$_{-10\%}$ condition was closest to an RD induced under EP$_{avg}$ conditions (marked by a white asterisk in the right panel of Fig. 6).

IV. DISCUSSION

In this study, we used computational models reconstructed from LGE-MRI scans of the fibrotic atria of individuals with PsAF to assess the sensitivity of AF-sustaining RD localization to variability in cell- and tissue-scale electrophysiological parameters and to patient-specific spatial

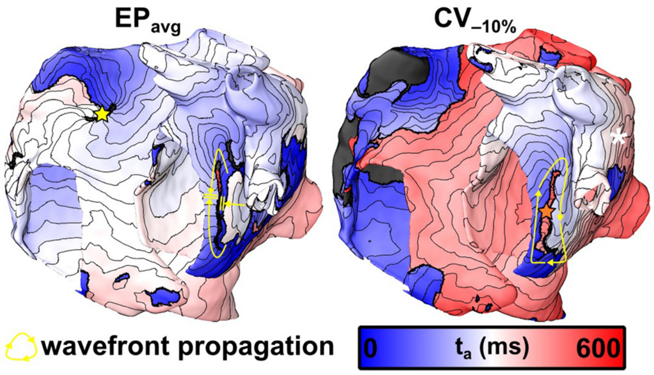

FIG. 6. Activation maps, following the same convention as Fig. 4, highlighting an example observed in the P02 model in which pacing induced RDs located in completely different atrial regions in simulations conducted under average human AF electrophysiology (EP$_{avg}$) conditions (region 5: inferior right atrium, near tricuspid valve annulus) and with −10% CV (region 1: left pulmonary veins). The latter RD was 33.96 mm from the location of the nearest RD from EP$_{avg}$ simulations (marked by asterisk), which was induced by a different pacing sequence than the one shown in the left-hand panel. See text for discussion of noteworthy features of wavefront propagation in EP$_{avg}$ model.

distribution of fibrotic tissues. To the best of our knowledge, this was the first attempt to systematically compare the contributions of the main structural and electrophysiological components of the fibrotic substrate in PsAF with respect to their influence on RD locations. We showed that: (1) in simulations conducted with ±10% APD/CV, a subset of RDs (∼35%–80%, depending on the EP variant) was observed in approximately the same locations as RDs observed in $\mathrm{EP}_{\mathrm{avg}}$ cases; (2) for the latter subset, the degree of overlap between RD targets in $\mathrm{APD/CV}_{\pm 10\%}$ and $\mathrm{EP}_{\mathrm{avg}}$ simulations was moderate (∼40%–60%) and approximately half of the inter-RD distances (d_{RD}) were within the diameter of one clinical ablation lesion (7 mm); (3) in many cases, where RD locations were robust to APD/CV variability, there were nonetheless differences in macroscopic arrhythmia features; and, (4) RDs induced in $\mathrm{APD/CV}_{\pm 10\%}$ models (∼20%–65%, depending on the EP variant) were sometimes observed in emergent locations (i.e., not observed in $\mathrm{EP}_{\mathrm{avg}}$ simulations), with average d_{RD} ranging from ∼20–40 mm.

A. Sensitivity of RD Localization to Variability in EP Parameters

Broadly speaking, the results presented in this study add depth to our growing understanding of how fibrotic remodeling in PsAF patients gives rise to a pro-arrhythmic substrate. Previously, we identified a particular spatial pattern of fibrotic tissues that strongly favored dynamic localization of RDs in patient-specific models.[7] Regions with this specific pattern corresponded to a subset of boundaries between fibrotic and non-fibrotic myocardium. This was consistent with the clinical descriptions of RD behavior observed in PsAF patients using non-invasive electrocardiographic imaging (ECGI), which indicated that organizing centers tend to cluster near boundaries between fibrotic and non-fibrotic tissues.[8] Our new findings present compelling evidence that these properties of RD localization are robust to electrophysiological variability, but with a very important caveat. Namely, RDs initiated in models with ±10% APD/CV still localize to boundaries between fibrotic and non-fibrotic tissues, but the particular distribution of preferential anchoring sites is sensitive to imposed electrophysiological variability. While some distinct RD sites are highly attractive (i.e., preserved across all EP parameter variants), others are observed only in $\mathrm{EP}_{\mathrm{avg}}$ simulations. Moreover, in nearly all atrial models considered, some RD sites only emerged upon modulation of APD and/or CV, suggesting that some potential RD ablation targets cannot be revealed using the current simulation protocol, i.e., applying burst pacing to the quiescent, non-ablated atrial model from a large (30–45) set of sites distributed evenly throughout the atria.

For many cases, in the subset of simulations, where RD localization was insensitive to EP variation and predominantly influenced by the spatial distribution of fibrotic tissues, APD/CV perturbations cause macroscopic changes in arrhythmia dynamics. We assessed these changes qualitatively by (A) identifying cases where RDs of opposite chirality had overlapping trajectories and (B) differences in activation sequence in regions distal to the RD trajectory (e.g., size and extent of conduction block areas, presence or absence of transient reentries, etc.) This is a key observation, since it suggests that changes in AF dynamics caused by APD/CV variability are not always consequential in terms of RD location, meaning that two episodes of AF that macroscopically appear completely different (i.e., via surface ECG inspection) may be driven by RDs in nearly identical locations.

Although the imposed EP parameter variations had the expected effects on the RD cycle length in general terms (i.e., a longer APD and a slower CV led to slower rotation, and abbreviated APD and accelerated CV led to faster rotation), the magnitude of those changes at the population level were smaller, particularly for $\mathrm{APD}_{+10\%}$ and $\mathrm{CV}_{-10\%}$ models (+1.8% and +0.1%, respectively). There is no simple explanation for the latter observation, since the cycle length of a particular RD can be affected by several factors in addition to intrinsic APD/CV. Notably, relative changes in the cycle length were much more pronounced for specific examples where RD trajectories were very similar between $\mathrm{EP}_{\mathrm{avg}}$ and $\mathrm{APD/CV}_{\pm 10\%}$ models (see annotations in Fig. 4). This suggests that in the absence of confounding factors (geometric structure, heterogeneity of fibrotic substrate, etc.) the effects of cell/tissue-scale changes in APD/CV on the RD cycle length are much more prominent.

Overall, our observations indicate that the structural component of the fibrotic substrate in PsAF patients remains a key factor in influencing RD localization dynamics, since trajectories are consistently observed in the vicinity of fibrotic tissue cluster boundaries, but the specific anchoring sites that emerge during AF simulations are sensitive to modulation in EP parameters. From a general clinical standpoint, this also reinforces the value of using LGE-MRI to acquire a detailed 3-dimensional description of each PsAF patient's fibrotic tissue distribution within the atrial anatomy prior to catheter ablation procedures, but stresses the importance of understanding how inter-patient differences in APD and CV may enhance or attenuate the arrhythmogenic propensity of certain fibrotic boundary regions observed via this approach.

B. Implications for Simulation-Based Planning of Catheter Ablation Procedures

Patient-specific computational modeling of PsAF has been proposed as a new approach to non-invasively develop personalized RD ablation strategies.[18,19,40,41] Previous studies have shown that such models are reconstructed from LGE-MRI scans that reveal the fibrotic tissue distribution in each individual's atria[42] and provide a non-invasive platform for analyzing the mechanistic underpinnings of RD dynamics.[7,22–24,43] The present study demonstrates that the level of uncertainty intrinsic to this type of atrial model is large enough that targeting simulation-predicted RD trajectories alone is not a reliable methodology for planning catheter ablation of PsAF. Although our results suggest that simulations conducted under $\mathrm{EP}_{\mathrm{avg}}$ conditions identified a subset of RD targets that were consistently observed under multiple different EP conditions, it is clear that the approach do not identify all possible targets. Instead, it may be necessary to combine direct targeting of RDs with other strategies based on targeting a specific subset of boundaries between non-fibrotic and fibrotic tissues, which may prove more robust to uncertainty.

C. Limitations

Our findings must be interpreted in the context of several noteworthy limitations. First, in order to assess the sensitivity of RD localization to EP parameter variation in a large population of atrial models with diverse spatial patterns of fibrotic tissues, we opted to consider a relatively limited subset of the parameter space of four discrete changes (±10% APD and ±10% CV). However, given the fact that our findings suggest that the specifics of RD localization behavior are sensitive to these changes, it is reasonable to assume that more dramatic changes would have a similar effect.

Second, our models do not incorporate intra-patient variability in CV due to specialized atrial structures, such as Bachmann's bundle, the crista terminals, and the pectinate muscles. Although our models include realistic atrial fiber orientations in the approximate vicinity of these structures, they cannot be delineated by clinical LGE-MRI and, as such, they are not modeled with distinct electrophysiology from other parts of the atria.

Third, as discussed in Methods, the parameter selection approach used in our study is limited by the fact that variations resulting in a certain APD/CV adjustment in a reduced scale and/or geometrically simplified models cannot be expected to result in emergent effects of the same magnitude at the organ scale. Future attempts to extend this work should include a detailed assessment of how cell- and tissue-scale parameter changes impact the dispersion of EP properties in image-based models of the fibrotic atria.

Finally, the mean RD cycle length observed in our $\mathrm{EP_{avg}}$ models was 278.6 ± 50.6 ms, and some RDs observed in our models had very long cycle lengths [e.g., ∼400 ms in Fig. 4(d)] compared to the clinically observed AF cycle length (AFCL), which is typically on the order of 180–250 ms. However, because AFCL is characterized electrocardiographically, it integrates effects from many different underlying factors including RD(s), sources of focal activation, and sinoatrial excitation. In contrast, our simulations are concerned exclusively with arrhythmias perpetuated by one RD at a time, which are induced by burst pacing electrically quiescent models in the absence of any other stimuli (including sinus rhythm). While this affords us the advantage of studying RD localization dynamics in the absence of all other confounding factors, in some cases, it results in an apparent discrepancy in between RD rotation rate and AFCL, which must be interpreted carefully.

D. Conclusions

In conclusion, we showed that RD localization in patient-specific computational models of PsAF is influenced by the morphology of each patient's unique spatial distribution of fibrotic atrial tissue and that changes in APD or CV can enhance or attenuate the likelihood that an RD will anchor to a specific site along the boundary between fibrotic and non-fibrotic tissues. In some cases, perturbing APD and CV by ±10% caused relatively little variation in RD trajectories, but in others, completely new RD sites that had never been seen under average EP conditions emerged.

As such, the level of uncertainty present in atrial models as constructed in the present study is sufficiently high that a personalized ablation strategy based on targeting simulation-predicted RD trajectories alone may not produce the desired result. More work is needed to determine whether this uncertainty can be overcome to facilitate simulation-based planning of catheter ablation procedures for PsAF patients.

SUPPLEMENTARY MATERIAL

The supplementary material contains 4 supplementary tables, which present comprehensive summary data for RDs observed in simulations conducted in all 12 atrial models under $\mathrm{APD/CV_{\pm 10\%}}$ conditions. It also contains 11 supplementary figures, which show the distribution of the fibrotic tissue and the degree of overlap between RD targets from $\mathrm{APD/CV_{\pm 10\%}}$ and $\mathrm{EP_{avg}}$ simulations for the 11 patient-specific atrial models not included in Fig. 3.

ACKNOWLEDGMENTS

This work was supported by American Heart Association 16-SDG-30440006 (to P.M.B.); by an NSF Graduate Research Fellowship and an ARCS Foundation Award (to S.Z.); and by the Johns Hopkins Medicine Discovery Fund and NIH DP1-HL123271 (to N.A.T.).

[1] H. Calkins, K. H. Kuck, R. Cappato, J. Brugada, A. J. Camm, S. A. Chen, H. J. Crijns, R. J. Damiano, Jr., D. W. Davies, J. DiMarco, J. Edgerton, K. Ellenbogen, M. D. Ezekowitz, D. E. Haines, M. Haissaguerre, G. Hindricks, Y. Iesaka, W. Jackman, J. Jalife, P. Jais, J. Kalman, D. Keane, Y. H. Kim, P. Kirchhof, G. Klein, H. Kottkamp, K. Kumagai, B. D. Lindsay, M. Mansour, F. E. Marchlinski, P. M. McCarthy, J. L. Mont, F. Morady, K. Nademanee, H. Nakagawa, A. Natale, S. Nattel, D. L. Packer, C. Pappone, E. Prystowsky, A. Raviele, V. Reddy, J. N. Ruskin, R. J. Shemin, H. M. Tsao, and D. Wilber, Heart Rhythm **9**(4), 632–696 (2012).

[2] M. H. Kim, S. S. Johnston, B. C. Chu, M. R. Dalal, and K. L. Schulman, Circ. Cardiovasc. Qual. Outcomes **4**(3), 313–320 (2011).

[3] S. Nattel, E. Guasch, I. Savelieva, F. G. Cosio, I. Valverde, J. L. Halperin, J. M. Conroy, S. M. Al-Khatib, P. L. Hess, P. Kirchhof, J. De Bono, G. Y. Lip, A. Banerjee, J. Ruskin, D. Blendea, and A. J. Camm, Eur. Heart J. **35**(22), 1448–1456 (2014).

[4] R. Mandapati, A. Skanes, J. Chen, O. Berenfeld, and J. Jalife, Circulation **101**(2), 194–199 (2000).

[5] M. Haissaguerre, M. Hocini, A. Denis, A. J. Shah, Y. Komatsu, S. Yamashita, M. Daly, S. Amraoui, S. Zellerhoff, M. Q. Picat, A. Quotb, L. Jesel, H. Lim, S. Ploux, P. Bordachar, G. Attuel, V. Meillet, P. Ritter, N. Derval, F. Sacher, O. Bernus, H. Cochet, P. Jais, and R. Dubois, Circulation **130**(7), 530–538 (2014).

[6] S. M. Narayan, D. E. Krummen, K. Shivkumar, P. Clopton, W. J. Rappel, and J. M. Miller, J. Am. Coll. Cardiol. **60**(7), 628–636 (2012).

[7] S. Zahid, H. Cochet, P. M. Boyle, E. L. Schwarz, K. N. Whyte, E. J. Vigmond, R. Dubois, M. Hocini, M. Haissaguerre, P. Jais, and N. A. Trayanova, Cardiovasc. Res. **110**(3), 443–454 (2016).

[8] H. Cochet, R. Dubois, S. Yamashita, N. Al Jefairi, B. Berte, J. Sellal, D. Hooks, A. Frontera, S. Amraoui, A. Zemmoura, A. Denis, N. Derval, F. Sacher, O. Corneloup, V. Latrabe, S. Clément-Guinaudeau, J. Relan, S. Zahid, P. M. Boyle, N. A. Trayanova, O. Bernus, M. Montaudon, F. Laurent, M. Hocini, M. Haissaguerre, and P. Jais, "Relationship between Fibrosis detected on Late Gadolinium-enhanced MRI and Reentrant Activity assessed with ECGI in Human Persistent Atrial Fibrillation," J Am. Coll. Cardiol. Clin. Electrophysiol. (in press).

[9] S. Nattel, J. Am. Coll. Cardiol. Clin. Electrophysiol. **3**(5), 425–435 (2017).

[10] N. F. Marrouche, D. Wilber, G. Hindricks, P. Jais, N. Akoum, F. Marchlinski, E. Kholmovski, N. Burgon, N. Hu, L. Mont, T. Deneke, M.

Duytschaever, T. Neumann, M. Mansour, C. Mahnkopf, B. Herweg, E. Daoud, E. Wissner, P. Bansmann, and J. Brachmann, JAMA **311**(5), 498–506 (2014).

[11]H. Cochet, A. Mouries, H. Nivet, F. Sacher, N. Derval, A. Denis, M. Merle, J. Relan, M. Hocini, M. Haissaguerre, F. Laurent, M. Montaudon, and P. Jais, J. Cardiovasc. Electrophysiol. **26**(5), 484–492 (2015).

[12]A. Harada, K. Sasaki, T. Fukushima, M. Ikeshita, T. Asano, S. Yamauchi, S. Tanaka, and T. Shoji, Ann. Thorac. Surg. **61**(1), 104–111 (1996).

[13]K. Lemola, M. Ting, P. Gupta, J. N. Anker, A. Chugh, E. Good, S. Reich, D. Tschopp, P. Igic, D. Elmouchi, K. Jongnarangsin, F. Bogun, F. Pelosi, Jr., F. Morady, and H. Oral, J. Am. Coll. Cardiol. **48**(2), 340–348 (2006).

[14]S. Lazar, S. Dixit, D. J. Callans, D. Lin, F. E. Marchlinski, and E. P. Gerstenfeld, Heart Rhythm **3**(8), 889–895 (2006).

[15]J. Sahadevan, K. Ryu, L. Peltz, C. M. Khrestian, R. W. Stewart, A. H. Markowitz, and A. L. Waldo, Circulation **110**(21), 3293–3299 (2004).

[16]D. M. Lombardo, F. H. Fenton, S. M. Narayan, and W. J. Rappel, PLoS Comput. Biol. **12**(8), e1005060 (2016).

[17]J. Andrade, P. Khairy, D. Dobrev, and S. Nattel, Circ. Res. **114**(9), 1453–1468 (2014).

[18]S. Zahid, K. N. Whyte, E. L. Schwarz, R. C. Blake 3rd, P. M. Boyle, J. Chrispin, A. Prakosa, E. G. Ipek, F. Pashakhanloo, H. R. Halperin, H. Calkins, R. D. Berger, S. Nazarian, and N. A. Trayanova, Heart Rhythm **13**(8), 1687–1698 (2016).

[19]P. M. Boyle, S. Zahid, and N. A. Trayanova, Europace **18**(suppl 4), iv136–iv145 (2016).

[20]I. M. Khurram, R. Beinart, V. Zipunnikov, J. Dewire, H. Yarmohammadi, T. Sasaki, D. D. Spragg, J. E. Marine, R. D. Berger, H. R. Halperin, H. Calkins, S. L. Zimmerman, and S. Nazarian, Heart Rhythm **11**(1), 85–92 (2014).

[21]F. Vadakkumpadan, H. Arevalo, C. Ceritoglu, M. Miller, and N. Trayanova, IEEE Trans. Med. Imaging **31**(5), 1051–1060 (2012).

[22]K. S. McDowell, F. Vadakkumpadan, R. Blake, J. Blauer, G. Plank, R. S. MacLeod, and N. A. Trayanova, J. Electrocardiol. **45**(6), 640–645 (2012).

[23]K. S. McDowell, F. Vadakkumpadan, R. Blake, J. Blauer, G. Plank, R. S. Macleod, and N. A. Trayanova, Biophys. J. **104**(12), 2764–2773 (2013).

[24]K. S. McDowell, S. Zahid, F. Vadakkumpadan, J. Blauer, R. S. MacLeod, and N. A. Trayanova, PLoS One **10**(2), e0117110 (2015).

[25]F. Pashakhanloo, D. A. Herzka, H. Ashikaga, S. Mori, N. Gai, D. A. Bluemke, N. A. Trayanova, and E. R. McVeigh, Circ.: Arrhythmia Electrophysiol. **9**(4), e004133 (2016).

[26]M. Courtemanche, R. J. Ramirez, and S. Nattel, Am. J. Physiol. **275**(1 Pt 2), H301–H321 (1998); available at http://ajpheart.physiology.org/content/275/1/H301.long.

[27]D. E. Krummen, J. D. Bayer, J. Ho, G. Ho, M. R. Smetak, P. Clopton, N. A. Trayanova, and S. M. Narayan, Circ.: Arrhythmia Electrophysiol. **5**(6), 1149–1159 (2012).

[28]S. Nattel, B. Burstein, and D. Dobrev, Circ.: Arrhythmia Electrophysiol. **1**(1), 62–73 (2008).

[29]D. Corradi, S. Callegari, R. Maestri, S. Benussi, and O. Alfieri, Nat. Clin. Pract. Cardiovasc. Med. **5**(12), 782–796 (2008).

[30]R. Kakkar and R. T. Lee, Circ. Res. **106**(1), 47–57 (2010).

[31]K. T. Konings, C. J. Kirchhof, J. R. Smeets, H. J. Wellens, O. C. Penn, and M. A. Allessie, Circulation **89**(4), 1665–1680 (1994).

[32]D. Li, S. Fareh, T. K. Leung, and S. Nattel, Circulation **100**(1), 87–95 (1999).

[33]B. Burstein, P. Comtois, G. Michael, K. Nishida, L. Villeneuve, Y. H. Yeh, and S. Nattel, Circ. Res. **105**(12), 1213–1222 (2009).

[34]F. H. Fenton, E. M. Cherry, H. M. Hastings, and S. J. Evans, Chaos **12**(3), 852–892 (2002).

[35]T. Krogh-Madsen, G. W. Abbott, and D. J. Christini, PLoS Comput. Biol. **8**(2), e1002390 (2012).

[36]J. N. Weiss, Z. Qu, and K. Shivkumar, Heart Rhythm **13**(9), 1868–1877 (2016).

[37]S. M. Narayan, D. E. Krummen, and W. J. Rappel, J. Cardiovasc. Electrophysiol. **23**(5), 447–454 (2012).

[38]E. J. Vigmond, F. Aguel, and N. A. Trayanova, IEEE Trans. Biomed. Eng. **49**(11), 1260–1269 (2002).

[39]E. J. Vigmond, M. Hughes, G. Plank, and L. J. Leon, J. Electrocardiol. **36**(Suppl), 69–74 (2003).

[40]J. D. Bayer, C. H. Roney, A. Pashaei, P. Jais, and E. J. Vigmond, Front Physiol. **7**, 108 (2016).

[41]P. M. Boyle, S. Zahid, and N. A. Trayanova, Expert Rev. Cardiovasc. Ther. **15**(5), 339–341 (2017).

[42]B. R. Parmar, T. R. Jarrett, N. S. Burgon, E. G. Kholmovski, N. W. Akoum, N. Hu, R. S. Macleod, N. F. Marrouche, and R. Ranjan, J. Cardiovasc. Electrophysiol. **25**(5), 457–463 (2014).

[43]C. H. Roney, J. D. Bayer, S. Zahid, M. Meo, P. M. Boyle, N. A. Trayanova, M. Haissaguerre, R. Dubois, H. Cochet, and E. J. Vigmond, Europace **18**(suppl 4), iv146–iv155 (2016).